The $Ca_V3.3$ calcium channel is the major sleep spindle pacemaker in thalamus

Simone Astori[a], Ralf D. Wimmer[a,b], Haydn M. Prosser[c,1], Corrado Corti[d,e], Mauro Corsi[d,e], Nicolas Liaudet[a], Andrea Volterra[a], Paul Franken[b], John P. Adelman[f], and Anita Lüthi[a,2]

[a]Department of Cell Biology and Morphology, University of Lausanne, CH-1005 Lausanne, Switzerland; [b]Center for Integrative Genomics, Génopode, University of Lausanne, CH-1015 Lausanne-Dorigny, Switzerland; [c]Genetics Research, GlaxoSmithKline Pharmaceuticals, New Frontiers Science Park, Harlow, Essex CM19 5AW, United Kingdom; [d]GlaxoSmithKline Neuroscience Centre for Excellence for Drug Discovery, 37129 Verona, Italy; [e]Aptuit Medicine Research Centre, 37129 Verona, Italy; and [f]Vollum Institute, Oregon Health and Science University, Portland, OR 97239

Edited by Rodolfo R. Llinas, New York University Medical Center, New York, NY, and approved July 13, 2011 (received for review April 18, 2011)

Low-threshold (T-type) Ca^{2+} channels encoded by the *Ca_V3* genes endow neurons with oscillatory properties that underlie slow waves characteristic of the non-rapid eye movement (NREM) sleep EEG. Three Ca_V3 channel subtypes are expressed in the thalamocortical (TC) system, but their respective roles for the sleep EEG are unclear. $Ca_V3.3$ protein is expressed abundantly in the nucleus reticularis thalami (nRt), an essential oscillatory burst generator. We report the characterization of a transgenic *$Ca_V3.3^{-/-}$* mouse line and demonstrate that $Ca_V3.3$ channels are indispensable for nRt function and for sleep spindles, a hallmark of natural sleep. The absence of $Ca_V3.3$ channels prevented oscillatory bursting in the low-frequency (4–10 Hz) range in nRt cells but spared tonic discharge. In contrast, adjacent TC neurons expressing $Ca_V3.1$ channels retained low-threshold bursts. Nevertheless, the generation of synchronized thalamic network oscillations underlying sleep-spindle waves was weakened markedly because of the reduced inhibition of TC neurons via nRt cells. T currents in *$Ca_V3.3^{-/-}$* mice were <30% compared with those in WT mice, and the remaining current, carried by $Ca_V3.2$ channels, generated dendritic $[Ca^{2+}]_i$ signals insufficient to provoke oscillatory bursting that arises from interplay with Ca^{2+}-dependent small conductance-type 2 K^+ channels. Finally, naturally sleeping *$Ca_V3.3^{-/-}$* mice showed a selective reduction in the power density of the σ frequency band (10–12 Hz) at transitions from NREM to REM sleep, with other EEG waves remaining unaltered. Together, these data identify a central role for $Ca_V3.3$ channels in the rhythmogenic properties of the sleep-spindle generator and provide a molecular target to elucidate the roles of sleep spindles for brain function and development.

inhibition | ion channel | Cacna1i | alpha1i | synchrony

The Ca^{2+} channels encoded by the *Ca_V3* genes activate near resting membrane potentials and generate low-threshold Ca^{2+} spikes leading to burst firing and low-frequency oscillatory discharge that are prominent in some thalamic, olivary, and cerebellar neurons (1). Among the low-threshold Ca^{2+} currents carried by Ca_V3 channels, those mediated by $Ca_V3.3$ channels are unique in that they display the slowest time course, the fastest recovery from inactivation, and often the most depolarized activation voltages (2, 3). Moreover, $Ca_V3.3$ mRNA is expressed predominantly in brain and shows highest regional specificity (3–5). To date, identification of specific physiological roles for $Ca_V3.3$ channels has been hampered for several reasons. First, these channels typically are coexpressed with $Ca_V3.1$ and/or $Ca_V3.2$ channels (4, 5), and specific pharmacological tools are not available (1). Second, $Ca_V3.3$ channels often are found in distal dendrites, limiting accessibility for electrophysiological characterization (6, 7). Finally, *$Ca_V3.3^{-/-}$* mice have not been reported, whereas *$Ca_V3.1^{-/-}$* and *$Ca_V3.2$* knockdown mice have helped address the roles of $Ca_V3.1$ and $Ca_V3.2$ channels in sleep and pain, respectively (8–10).

In the thalamus, $Ca_V3.3$ mRNA and protein are abundant in GABAergic cells of the surrounding nucleus reticularis thalami (nRt), the principal source of inhibition to relay nuclei, whereas excitatory thalamocortical (TC) neurons are not immunopositive for $Ca_V3.3$ (4, 5, 11). The slow decay and the depolarized activation range of low-threshold Ca^{2+} currents in the nRt (12) are thought to reflect the dominant mRNA expression of $Ca_V3.3$ over $Ca_V3.2$ channels (5, 7, 13). Vigorous bursting properties in nRt underlie its well-documented role in pacemaking sleep spindles (14) and its proposed involvement in attentional gating mechanisms (15). Therefore, the nRt is ideally suited to explore the cellular and circuit roles of $Ca_V3.3$ channels.

Here, we describe the *$Ca_V3.3^{-/-}$* mouse and report that $Ca_V3.3$ channels are required for nRt cell bursting and for synchronized rhythmicity in intrathalamic circuits. *$Ca_V3.3^{-/-}$* mice show selectively weakened spindle wave generation during spontaneous sleep. These results establish a specific role for $Ca_V3.3$ channels in a sleep EEG hallmark and, more generally, an animal model to provide insight into sleep's role for the brain.

Results

Generation of *$Ca_V3.3^{-/-}$* Mice. Interruption of the *$Ca_V3.3$* gene was achieved through homologous recombination in 129Ola ES cells. The targeting construct deleted a 6.8-kb genomic region (National Center for Biotechnology Information m37 15:80,198, 299-80,205,160) encoding exons 11–21, replacing them with a β-galactosidase–neomycin cassette (Fig. 1*A*). The engineered allele deletes the coding sequence between the predicted IIS2 and IIIS4 transmembrane regions, including the third predicted intracellular domain (3). Additionally, exons 10 and 22 are out of the translational reading frame; therefore, any truncated protein product will not be functional. *$Ca_V3.3$* gene deletion was confirmed by RT-PCR experiments using RNA extracted from cerebellum, olfactory bulb, cortex, and thalamus (Fig. 1*B*). The deletion of the *$Ca_V3.3$* gene did not affect transcription of the *$Ca_V3.2$* gene in thalamus, as assessed by quantitative RT-PCR (Fig. 1*C*). For all experiments described below, mouse genotype was determined by PCR (Fig. 1*D*), and homozygous *$Ca_V3.3^{-/-}$* and WT littermates were used.

nRt Oscillatory Burst Discharges Are Impaired in *$Ca_V3.3^{-/-}$* Mice. Whole-cell current-clamp recordings were obtained from nRt cells in acute brain slices of 3- to 4-wk-old mice. The oscillatory bursting characteristic for nRt cells was elicited at the offset of brief membrane hyperpolarizations, whereas tonic discharges

Author contributions: S.A., R.D.W., P.F., and A.L. designed research; S.A., R.D.W., H.M.P., C.C., and M.C. performed research; N.L. and A.V. contributed new reagents/analytic tools; S.A. and R.D.W. analyzed data; and S.A., R.D.W., J.P.A., and A.L. wrote the paper.

The authors declare no conflict of interest.

This article is a PNAS Direct Submission.

[1]Present address: The Wellcome Trust Sanger Institute, Wellcome Trust Genome Campus, Hinxton, Cambridge CB10 1SA, United Kingdom.

[2]To whom correspondence should be addressed. E-mail: anita.luthi@unil.ch.

This article contains supporting information online at www.pnas.org/lookup/suppl/doi:10.1073/pnas.1105115108/-/DCSupplemental.

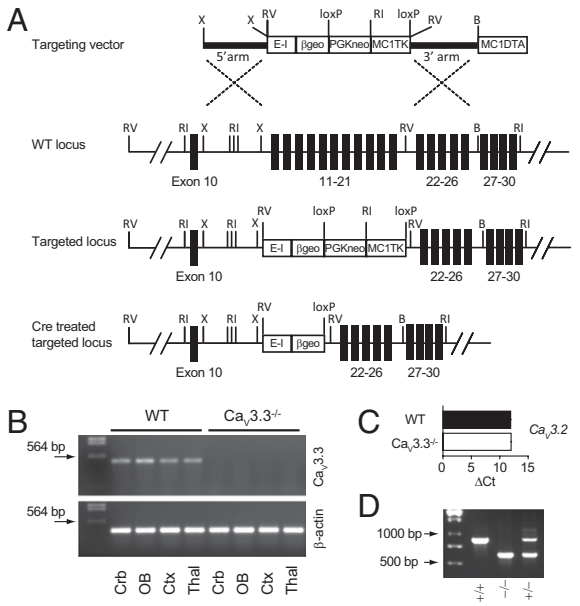

Fig. 1. Gene targeting of the *$Ca_V3.3$* locus. (*A*) Restriction enzyme map of the targeting vector, the WT locus, and the predicted mutant *$Ca_V3.3$* allele following homologous recombination and after Cre deletion of the selection cassette in the finalized allele used to create mice. Only restriction sites relevant to the targeting strategy are indicated. The exon/intron numbering is as described in Mouse Genome Information (Vertebrate Genome Annotation). The sizes of exons and introns are not to scale. Restriction enzymes: B, BamHI; RI, EcoRI; RV, EcoRV; X, Xho1. Cassettes: βgeo, β-galactosidase-neomycin; E-I, EN2-SA-internal ribosomal entry site; MC1DTA, diphtheria toxin A fragment gene driven by an MC1 promoter; MC1TK, thymidine kinase gene; PGKneo, phosphoglycerol kinase-neomycin. (*B*) RT-PCR for $Ca_V3.3$ mRNA and β-actin from different brain areas, as indicated, in WT and *$Ca_V3.3^{-/-}$* mice. Crb, cerebellum; Ctx, cortex; OB, olfactory bulb; Thal, thalamus. (*C*) RT-PCR of thalamic $Ca_V3.2$ expression indicated as mean cycle of threshold differences between $Ca_V3.2$ and GAPDH mRNA (WT, $n = 6$; $Ca_V3.3^{-/-}$, $n = 6$). (*D*) PCR analysis of tail DNA to identify WT, heterozygous, and homozygous animals. PCR primers used are identified in *SI Materials and Methods*.

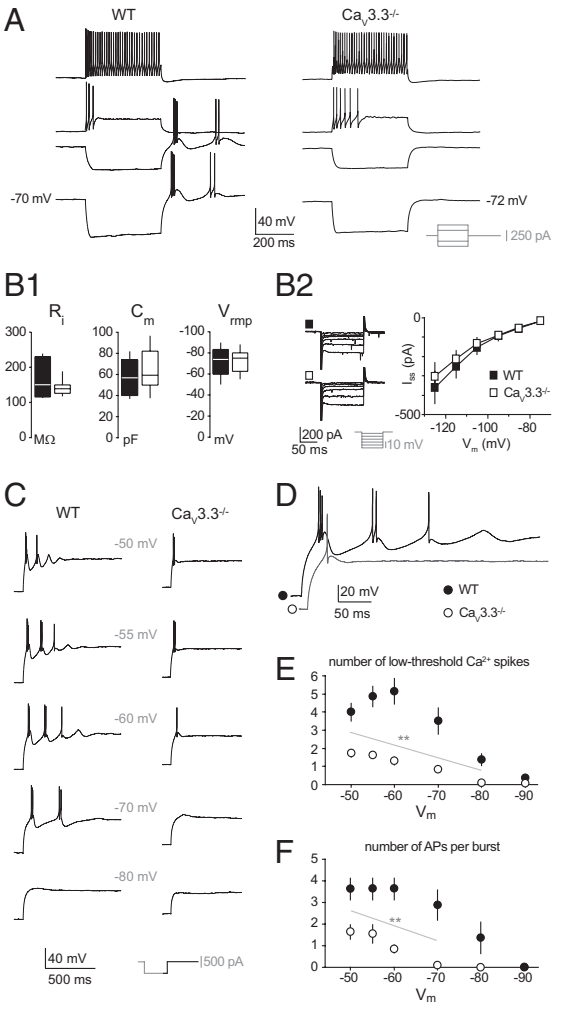

Fig. 2. $Ca_V3.3$ T-type Ca^{2+} channel deletion impairs rebound bursting in nRt cells. (*A*) Representative discharge patterns in nRt cells of a WT and a *$Ca_V3.3^{-/-}$* mouse induced by step current injections from rest. (*Inset*) Protocol. (*B*1) Box-and-whisker plots of input resistance (R_i), membrane capacitance (C_m), and resting membrane potential (V_{rmp}) of nRt cells from WT mice ($n = 8$) and *$Ca_V3.3^{-/-}$* mice ($n = 13$). For each box, the midline indicates the median, and top and bottom lines indicate 90th and 10th percentiles, respectively; whiskers span maximal to minimal values ($P > 0.05$ in all cases). (*B2*) (*Left*) Current responses to increasing hyperpolarizing voltage steps. (*Inset*) Protocol. (*Right*) Average values of steady-state current (I_{ss}) at voltages indicated (WT, $n = 7$; $Ca_V3.3^{-/-}$, $n = 6$; $P > 0.05$). (*C*) Membrane voltage responses to −500-pA–step current injections from different holding potentials, as indicated. (*D*) Expanded traces from *C* (−60 mV). (*E* and *F*) Number of low-threshold Ca^{2+} spikes (*E*) and number of APs (*F*) within the first burst differed across a wide range of membrane potentials (WT, $n = 8$; $Ca_V3.3^{-/-}$, $n = 13$; $^{**}P < 0.01$).

were generated upon depolarization from the resting membrane potential of −70 mV (16). In contrast, in nRt cells from *$Ca_V3.3^{-/-}$* mice, repetitive burst discharges were absent, whereas tonic firing was unaltered (Fig. 2*A* and Table S1). Passive membrane properties did not differ between genotypes ($P > 0.05$ in all cases) (Fig. 2*B*1). Additionally, no difference was observed in inwardly rectifying currents ($P > 0.05$) (Fig. 2*B*2) (17).

We next attempted to facilitate rhythmic bursting by imposing transient hyperpolarizations from more depolarized membrane potentials (Fig. 2 *C–F*). Low-threshold Ca^{2+} spikes could be elicited in *$Ca_V3.3^{-/-}$* nRt cells that were depolarized beyond −60 mV before transient hyperpolarization; however, the number of Ca^{2+} spikes was reduced markedly compared with WT cells (e.g., at −55 mV, 4.9 ± 0.6 in WT, $n = 8$, vs. 1.6 ± 0.2 in $Ca_V3.3^{-/-}$, $n = 13$; $P < 0.01$) (Fig. 2 *D* and *E*). Moreover, *$Ca_V3.3^{-/-}$* cells typically generated a single low-threshold Ca^{2+} spike crowned with action potentials (APs), whereas APs were triggered for several Ca^{2+} spikes in WT cells (Fig. 2*D*). Finally, the number of APs generated by the first Ca^{2+} spike was diminished markedly (e.g., at −55 mV, 3.6 ± 0.5 in WT vs. 1.5 ± 0.4 in $Ca_V3.3^{-/-}$; $P < 0.01$) (Fig. 2*F*). Indeed, in 7 of 13 cells, only a single or no AP could be elicited across the range of voltages tested, indicating that full-fledged burst discharge failed. The rebound depolarization observed in *$Ca_V3.3^{-/-}$* cells was blocked by low Ni^{2+} concentrations (50–100 μM in bath) (Fig. S1), indicating that a T-type conductance remained. Similar discharge deficits were found in 10-wk-old animals (Fig. S2).

In contrast to the drastic reduction of bursting in nRt cells, T channel-mediated burst discharge was preserved in TC cells principally expressing $Ca_V3.1$ channels, and low-threshold Ca^{2+} spikes were crowned by a comparable number of APs (Fig. 3 *A–C*).

Inhibitory synaptic output from bursting nRt cells is important for rebound burst generation in connected TC cells. To test whether the absence of $Ca_V3.3$ channels affected nRt-mediated inhibition of TC cells, we recorded synaptic responses in voltage-clamped TC cells evoked by stimulating excitatory afferents onto nRt cells (6). In WT mice, synaptic responses typically appeared as multipeak events with an interpeak interval of 4.2 ± 0.5 ms (in six of seven cells) that is characteristic for the high-frequency

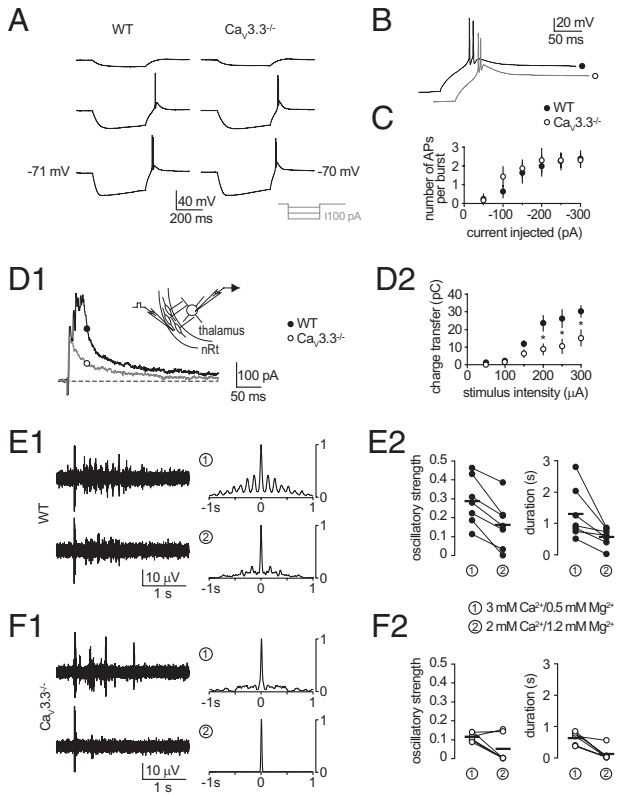

Fig. 3. *$Ca_V3.3$* deletion does not affect rebound discharge in TC cells but reduces intrathalamic synchronized network activity. (*A*) Representative traces of rebound bursting in TC cells. (*Inset*) Protocol. (*B*) Expanded overlay of traces shown in *A* (−250-pA steps). (*C*) The number of APs within the burst did not differ across the whole range of current injections tested (WT, $n = 8$; $Ca_V3.3^{-/-}$, $n = 7$; $P > 0.05$). (*D1*) Synaptic responses evoked in TC cells by electrical stimulation in nRt. (*Inset*) Recording configuration. (*D2*) Synaptic responses in TC cells show a larger charge transfer in WT cells at the stimulus intensities at which responses could be evoked reliably (WT, $n = 7$; $Ca_V3.3^{-/-}$, $n = 6$; $P < 0.05$). (*E1*) Representative multiunit discharges in nRt from WT mice. Circled numbers indicate Ca^{2+}/Mg^{2+} in ACSF. Traces are aligned to stimulus artifacts. (*E2*) Oscillatory strength and duration of spindles were calculated from autocorrelograms as ratio of second to first peak and as time between 100% and 5% of the maximum, respectively. Values from single experiments (circles) and average values (horizontals bars) are displayed for the two ionic conditions ($n = 7$). (*F1* and *F2*) As in *E1* and *E2* for $Ca_V3.3^{-/-}$. In four of six cases, change in Ca^{2+}/Mg^{2+} completely abolished oscillations.

bursts of nRt cells (Fig. 3*D*1). In contrast, in $Ca_V3.3^{-/-}$ mice, multiple peaks appeared rarely (in two of six cells). As a result, the inhibitory driving force onto TC cells was significantly smaller in $Ca_V3.3^{-/-}$ mice, as determined from the integral of synaptic currents evoked by increasing stimulus intensities (e.g., with 250-μA stimulus intensity: 26 ± 5 pC in WT mice vs. 10 ± 4 pC in $Ca_V3.3^{-/-}$ mice; $P < 0.05$) (Fig. 3*D*2).

To investigate the effects of reduced nRt inhibitory drive on intrathalamic circuitry involved in sleep spindles (18), we examined synchronized multiunit discharges in nRt elicited via bipolar electrical stimulation of excitatory afferents in the adjacent internal capsule and perpetuated via reciprocal synaptic interactions with TC cells. To facilitate network activity, we first perfused slices with artificial CSF (ACSF) containing increased Ca^{2+} (3 mM) and decreased Mg^{2+} (0.5 mM). In WT mice, robust reverberating activity at 7–9 Hz lasting ∼1.5 s was elicited (Fig. 3*E*). Similar activity was detected in slices from $Ca_V3.3^{-/-}$ mice, but with weaker oscillatory strength ($P < 0.05$) and shorter duration ($P = 0.07$) (Fig. 3 *E* and *F*). Notably, after returning to normal divalent cation concentrations (2 mM Ca^{2+}/1.2 mM Mg^{2+}), synchronized oscillations disappeared in $Ca_V3.3^{-/-}$ mice in most cases (four of six slices) but remained in WT slices (six of seven slices). Thus, the absence of $Ca_V3.3$ channels impairs the capability of the nRt–TC network to generate spindle-like discharge, but rhythmic discharge can be restored partially by increasing cellular excitability.

Dominant Contribution of $Ca_V3.3$ Channels to T Currents in nRt Neurons. Whole-cell T currents were elicited by increasingly depolarized voltage steps (1 s) from −100 mV using a fluoride-containing patch pipette solution (Fig. 4 and *SI Materials and Methods*). Compared with WT cells, T-current density in $Ca_V3.3^{-/-}$ nRt cells was reduced throughout the activation range (e.g., 78% reduction at −70 mV; $P < 0.01$, and 54% reduction at −50 mV; $P < 0.01$; $n = 10$ for WT and $n = 8$ for $Ca_V3.3^{-/-}$) (Fig. 4*A*2). Moreover, the activation curve was shifted toward more depolarized potentials in $Ca_V3.3^{-/-}$ mice ($P < 0.01$) (Fig. 4*A*3). Strikingly, T currents from $Ca_V3.3^{-/-}$ cells had a 2.5-fold faster decay than WT cells (e.g., at −50 mV $\tau_{w,\,decay} = 96 \pm 10$ ms for WT vs. $\tau_{w,\,decay} = 38 \pm 6$ ms for $Ca_V3.3^{-/-}$; $n = 10$ and 8, respectively; $P < 0.01$) (Fig. 4*B*). Similar alterations were found at near-physiological temperature (Fig. S3). Notably, recovery from steady-state inactivation was retarded in $Ca_V3.3^{-/-}$ cells (time constant of recovery: $\tau_{w,\,rec} = 1.5 \pm 0.3$ s for WT vs. $\tau_{w,\,rec} = 7.9 \pm 2.3$ s for $Ca_V3.3^{-/-}$; $n = 10$ and 8, respectively; $P < 0.05$) (Fig. 4*C*).

Pharmacological properties of T currents in WT and $Ca_V3.3^{-/-}$ cells were compared for current block by Ni^{2+}, which differs between $Ca_V3.2$ and $Ca_V3.3$ channels (Fig. 4*D*) (19). In $Ca_V3.3^{-/-}$ cells, T currents were strongly reduced with 50 μM Ni^{2+} (by 74 ± 7%; $n = 6$; $P < 0.01$), but 200 μM Ni^{2+} blocked T currents only partially in WT cells (by 40 ± 5%; $n = 6$; $P < 0.01$), and a residual current remained even with 500 μM Ni^{2+} (peak reduction: 60 ± 4%; $n = 6$; $P < 0.01$). Similar blockade was found with an intracellular solution that preserves cellular discharge properties (Fig. S4). Additionally, low-threshold Ca^{2+} currents evoked in $Ca_V3.3^{-/-}$ cells were invariant against the R-type channel blocker SNX-482 (change by −1.0 ± 2.9%; $n = 4$, $P > 0.05$) (Fig. S4) at doses that reduce R currents in nRt slices (20). Around resting membrane potentials, low-threshold Ca^{2+} currents thus are carried dominantly by T channels in WT nRt cells and contain two components with different Ni^{2+} sensitivity (13).

Elimination of Burst-Mediated Dendritic Ca^{2+} Signaling in $Ca_V3.3^{-/-}$ Neurons. $Ca_V3.3$ channels have been implicated previously in intracellular $[Ca^{2+}]_i$ dynamics important for cellular rhythmicity (16, 21). We performed fluorescent imaging in cells infused with the Ca^{2+}-sensitive dye bis-fura-2 (1 mM) and focused on transients in dye-bound intracellular Ca^{2+} concentrations ($\Delta[Ca^{2+}]_i$) in nRt dendrites, which are essential for oscillatory bursting (16). Fluorescent signals were collected from portions of dendritic arbors up to ∼200 μm from the cell body (Fig. 5 *A* and *B*). In cells from WT mice, repetitive burst firing induced by brief hyperpolarizing steps evoked large $\Delta[Ca^{2+}]_i$ (Fig. 5*A*). In contrast, in cells from $Ca_V3.3^{-/-}$ mice, rebound firing, even when facilitated by prior membrane depolarization, produced only a minor $\Delta[Ca^{2+}]_i$, with peak amplitudes of $\Delta[Ca^{2+}]_i$ reduced by ∼80% compared with WT (Fig. 5*B*). Tonic firing elicited by depolarizing steps evoked comparable $\Delta[Ca^{2+}]_i$ in both genotypes, indicating intact function of high-voltage–activated (HVA) Ca^{2+} channels.

Coupling between T channels and Ca^{2+}-dependent small conductance-type 2 K^+ (SK2) channels in nRt dendrites underlies oscillatory discharge of nRt cells (16). We used the SK channel blocker apamin to assess whether the absence of $Ca_V3.3$ channels disrupted this coupling, which manifests as a biphasic current containing inward T- and outward SK2-current components (Fig. 5*C*) (16). Apamin-sensitive SK currents, obtained via digital subtraction of whole-cell currents in apamin from those in control

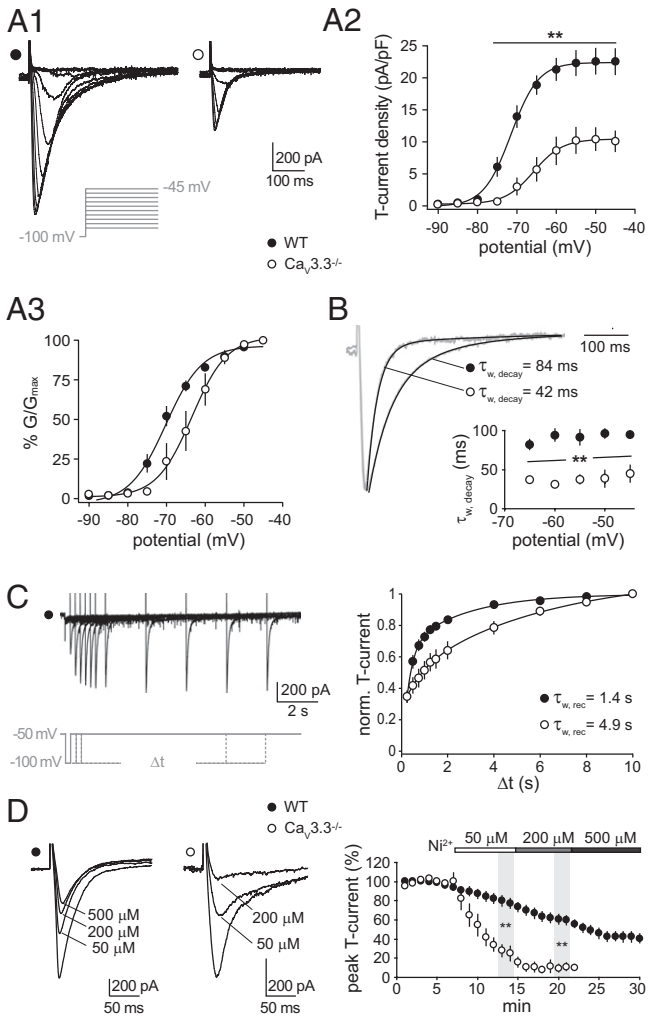

Fig. 4. $Ca_V3.3$ channels determine T-current characteristics in nRt cells. (*A1*) Families of isolated T currents evoked in WT and $Ca_V3.3^{-/-}$ cells. (*Inset*) Protocol. (*A2*) T-current density calculated by normalizing peak currents to cell capacitance (WT, n = 10; $Ca_V3.3^{-/-}$, n = 8). (*A3*) Activation curve of T currents (estimated V_{half} = −70.4 ± 1.0 mV for WT vs. V_{half} = −63.6 ± 1.9 mV for $Ca_V3.3^{-/-}$; n = 10 and 8, respectively). (*B*) Scaled-to-peak traces reveal faster decay kinetics in $Ca_V3.3^{-/-}$ mice. Plot displays average values of $\tau_{w,\ decay}$, calculated from double-exponential fit (WT, n = 10; $Ca_V3.3^{-/-}$, n = 8). (*C*) (*Left*) Example of a recording of recovery from steady-state inactivation in a WT nRt cell, with the voltage-clamp protocol indicated below. (*Right*) Time course of recovery from inactivation, with T-current peaks normalized to that obtained for Δt = 10 s. Recovery time constants ($\tau_{w,\ rec}$) were obtained from double-exponential fits (WT, n = 10; $Ca_V3.3^{-/-}$, n = 8). (*D*) (*Left*) Representative traces of T currents with increasing Ni^{2+}. (*Right*) Average time course shows higher sensitivity of $Ca_V3.3^{-/-}$ cells to Ni^{2+} (WT, n = 6; $Ca_V3.3^{-/-}$, n = 6). For all plots in this figure, $^{**}P < 0.01$.

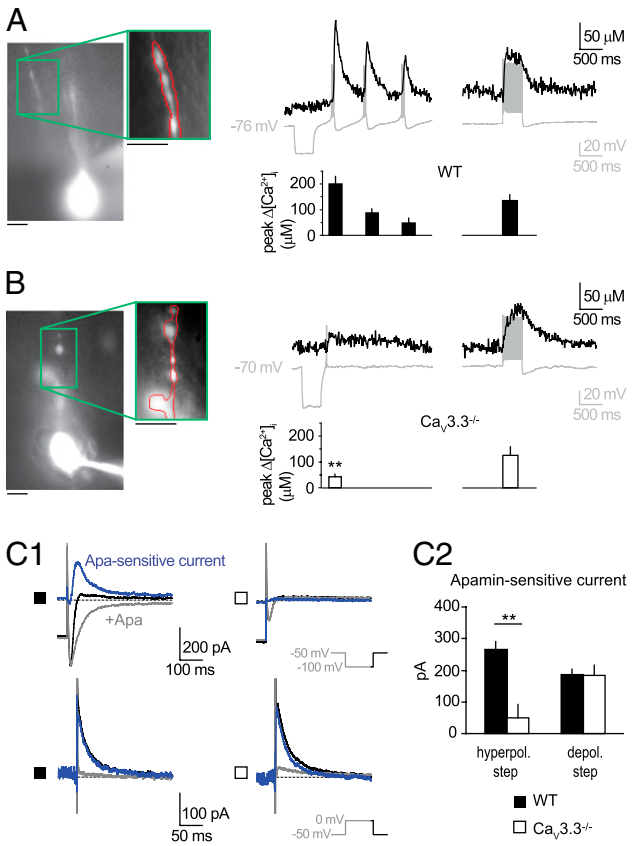

Fig. 5. Impaired Ca^{2+} signaling in $Ca_V3.3^{-/-}$ mice. (*A*) Example of $[Ca^{2+}]_i$ transients (black) evoked in a WT nRt cell mediated by rebound bursting or tonic firing (gray). Fluorescent signals were collected in a dendritic region (enlarged image). The photograph of the fluorescent cell was taken at the end of the recording session and with increased illumination intensity. Bar graphs are aligned to raw traces and show summary data (n = 8) for each peak $\Delta[Ca^{2+}]_i$ for rebound bursting and tonic firing. (Scale bars: 5 μm.) (*B*) As in *A*, for a $Ca_V3.3^{-/-}$ mouse (n = 8). In $Ca_V3.3^{-/-}$ mice, only cells displaying rebound spiking were considered. $^{**}P < 0.01$ compared with corresponding WT signal. (*C1*) SK2 currents evoked by voltage protocols shown in *Insets*. The last portions of a 125-ms voltage step and the following 500 ms are displayed. Control, black; apamin (Apa), gray; apamin-sensitive currents (blue) were generated by digital subtraction. (*C2*) Summary data (WT, n = 7; $Ca_V3.3^{-/-}$, n = 9; $^{**}P < 0.01$).

(16), were strongly reduced when evoked via T currents (265 ± 26 pA in WT vs. 50 ± 4 pA in $Ca_V3.3^{-/-}$; n = 7 and 9, respectively; $P <$ 0.01) but not when activated via HVA Ca^{2+} currents (188 ± 16 pA in WT vs. 185 ± 32 pA in $Ca_V3.3^{-/-}$; n = 7 and 9, respectively; $P >$ 0.05). Notably, the reduction (~80%) in SK2 current was not in proportion to the T-current amplitudes remaining in the $Ca_V3.3^{-/-}$ nRt cells (~40%) recorded for this series (average peak amplitude: 250 ± 117 pA in $Ca_V3.3^{-/-}$ vs. 591 ± 81 pA in WT). Therefore, to obtain a coupling index, we quantified the ratio between the apamin-sensitive SK2 current and the net T current for every cell. This ratio approached zero in $Ca_V3.3^{-/-}$ cells (0.5 ± 0.1 in WT vs. 0.03 ± 0.17 in $Ca_V3.3^{-/-}$; $P <$ 0.05). Thus, $Ca_V3.3$ channels are indispensable for the coupling between T channels and SK2 channels in nRt cells.

Impaired Spindle Generation During Natural Sleep in $Ca_V3.3^{-/-}$ Mice. Repetitive nRt low-threshold bursting is vigorous during natural sleep (14, 18). To test how the impaired activity of nRt cells in $Ca_V3.3^{-/-}$ mice affected sleep physiology, we performed polysomnographic recordings in freely moving mice with chronically implanted EEG and electromyography (EMG) electrodes (WT, n = 8; $Ca_V3.3^{-/-}$, n = 7). These recordings yielded the typical non-rapid eye movement (NREM) sleep power spectrum dominated by a peak in the δ range (0.75–4 Hz) and a small contribution in the σ range (10–12 Hz), both of which were unaffected by the absence of $Ca_V3.3$ channels (Fig. 6*A*). Because sleep spindles contribute dominantly to the σ range at NREM-to-REM sleep transitions but represent a minor component in the spectral profile of total time spent in NREM sleep (22), we next focused on the surge of σ power (10–12 Hz) peaking ~30 s before REM sleep onset. This analysis has proven useful in assessing deficits related to nRt bursting (16, 23). Indeed, the surge in σ power was reduced significantly in $Ca_V3.3^{-/-}$ mice (at peak: WT,

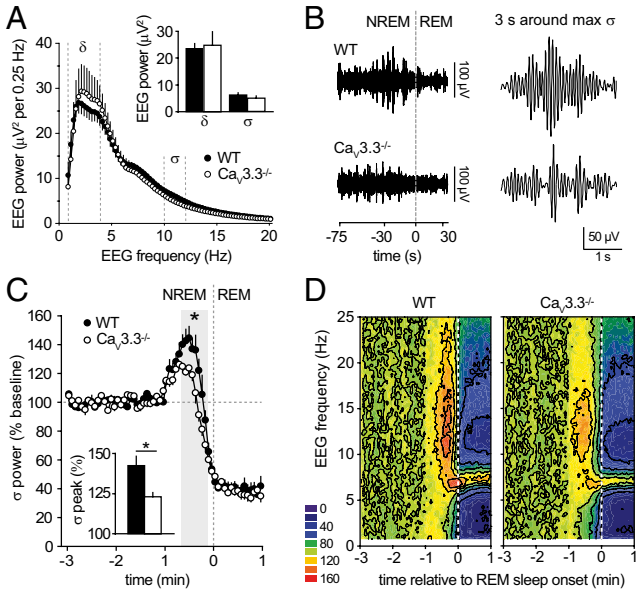

Fig. 6. Selective reduction in EEG σ power in naturally sleeping $Ca_V3.3^{-/-}$ mice. (*A*) Spectral analysis of the absolute EEG power between 0.75 and 20 Hz for NREM sleep. Dotted lines delineate δ (0.75–4 Hz) and σ (10–12 Hz) bands. (*Inset*) Mean absolute δ and σ power. (*B*) (*Left*) Example of traces of band pass-filtered (10–12 Hz) EEG recordings illustrating the surge of spindle power at NREM-to-REM sleep transitions. (*Right*) Zoom-in on the maximal σ activity before the transition. (*C*) Time course of mean EEG activity in the σ frequency band at NREM-to-REM sleep transitions. Data were normalized to the average σ power in the time window −3 to −1 min. Gray box indicates data points with significant difference (*$P < 0.05$) between groups. (*Inset*) Peak values of σ power at the surge before REM sleep onset. (*D*) Color-coded heat map of percent EEG power between 0.75–25 Hz (0.25-Hz bins) during the NREM-to-REM sleep transition. Contour lines connect levels of similar relative power in nine color–coded 20% increments. White dashed lines at time 0 indicate NREM/REM sleep border.

143 ± 7% vs. $Ca_V3.3^{-/-}$, 120 ± 4%; $P < 0.05$) (Fig. 6 *B* and *C*), but absolute σ power baseline values did not differ (WT, 6.1 ± 0.9 μV^2 vs. $Ca_V3.3^{-/-}$, 4.8 ± 0.8 μV^2, $P > 0.05$). The decrement of δ power at the transition was unaffected ($P > 0.05$) (Fig. 6*D*), and absolute δ power baseline values were similar (WT, 24.6 ± 2.0 μV^2 vs. $Ca_V3.3^{-/-}$, 25.4 ± 5.2 μV^2, $P > 0.05$). Deficits in nRt bursting thus manifest specifically at the level of a single sleep EEG frequency band.

Discussion

The present results demonstrate an obligatory role for $Ca_V3.3$ channels in burst discharge of cells in the nRt, a long-established pacemaker element in the genesis of the EEG characteristics for slow-wave sleep. We also identify $Ca_V3.3$ channels as the Ca^{2+} source necessary for dendritic Ca^{2+} transients and for the coupling to SK2 channels that underlies the oscillatory bursting of nRt cells. Finally, $Ca_V3.3$ channels are essential for spindle generation during natural sleep, with other frequency bands remaining untouched. Together, the $Ca_V3.3$ channel represents a specific molecular link between a special type of neuronal discharge and an EEG hallmark of sleep.

The unique kinetic properties of $Ca_V3.3$-mediated currents (2, 3) made these channels candidates to underlie the strong burst discharge properties of nRt cells (24). Several of our findings now show directly that $Ca_V3.3$ channels in nRt mediate native current characteristics. First, the absence of $Ca_V3.3$ channels accelerated the decay of the remaining current, indicating that the characteristic slow decay of whole-cell T currents in nRt is dependent on $Ca_V3.3$ channels. Also, in $Ca_V3.2^{-/-}$ nRt cells recorded with similar intracellular recording solutions (13), decay kinetics were comparable to the ones we obtained in WT cells. Second, recovery from inactivation of the T current was slowed in the absence of $Ca_V3.3$ channels, consistent with the rapid recovery of cloned $Ca_V3.3$ channels (2). Finally, Ni^{2+} sensitivity was low in the WT cells but increased dramatically in the absence of $Ca_V3.3$ channels, suggesting that a weakly Ni^{2+}-sensitive Ca^{2+} current dominates in WT, whereas a highly Ni^{2+}-sensitive Ca^{2+} current remained in the $Ca_V3.3^{-/-}$ nRt cells. This pharmacological profile points to a T-current component carried by $Ca_V3.2$ channels, consistent with previous observations in $Ca_V3.2^{-/-}$ mice (13). We found that $Ca_V3.3$ currents were largely responsible for cellular bursting, for dendritic Ca^{2+} signals, and for the coupling to SK2 channels, consistent with their predominant dendritic expression (11). However, network activity could be sustained in $Ca_V3.3^{-/-}$ nRt cells, and whether $Ca_V3.2$ channel activity in nRt contributes to and plays a role in the regulation of natural sleep is not yet known.

Since Morison and Bassett's original observation that spindle oscillations in thalamus resist decortication (25), decades of research have established the recurrent thalamic circuits as their site of origin (14). In contrast, how thalamic oscillators shape the two other major NREM sleep frequency bands, the slow rhythm (<1 Hz) and the δ waves (0.5–4 Hz), remains unknown, although nRt bursting has been implicated (14, 26). In particular, δ waves are suppressed in mice lacking either SK2- or $K_V3.1/3.3$-type K^+ channels, both of which are important for rhythmic bursting in nRt (16, 27). The present results help clarify the intertwined roles of cortical and thalamic oscillators in the sleep EEG. First, they establish a specific role for nRt bursting as the core mechanism for spindle waves, thus providing a genetic basis for the widely acknowledged unique standing of nRt in this characteristic sleep rhythm. The presence of $Ca_V3.3$ protein close to asymmetric synapses (11) also underscores the fact that corticothalamic excitatory input can trigger local nRt bursting (6) and recruit thalamus into large-scale brain oscillations (14). Second, they demonstrate a minor role, if any, for nRt bursting in low-frequency (<4 Hz) EEG waves of natural sleep, suggesting a major cortical contribution to these rhythms. This result is consistent with the established cortical origin of slow rhythms (14) but remains intriguing in the case of δ waves, for which nRt acts as an intrathalamic synchronizing element (14). Monitoring intrathalamic and cortical activity during deep sleep will be required to resolve the relation between thalamic and cortical contributions to δ waves. It also must be considered that $Ca_V3.2$ and $Ca_V3.3$ channels are both expressed in cortex (4, 11), and the absence of $Ca_V3.3$ channels from birth might alter cortical network activity chronically. This alteration, in turn, can promote low-frequency burst discharge in pyramidal neurons, perhaps by up-regulation of $Ca_V3.2$ expression (28). Moreover, marked adaptive plasticity occurs in nRt in response to cortical injury (17), leading to augmented excitatory input in uninjured corticothalamic fibers. The current results show that thalamic cellular properties, in particular $Ca_V3.2$ channels in nRt, are largely spared from compensatory alterations when $Ca_V3.3$ is removed, but compensations at synaptic and circuit levels remain to be explored.

Sleep spindles contribute to brain plasticity both in adulthood and during development (29, 30). Spindle waves are implicated in sleep-dependent memory consolidation by coordinating information transfer from hippocampus to cortex (29). Moreover, mimicking spindle activity in cortical cells promotes associative synaptic plasticity (31). In the developing brain, local cortical spindles probably involving thalamus are the first indications of synchronized network activity (30). Further analysis of the $Ca_V3.3^{-/-}$ mouse undoubtedly will be essential in delineating the role of thalamically generated spindles in these diverse brain processes.

Materials and Methods

Generation of $Ca_V3.3^{-/-}$ Mice. Gene targeting was performed in E14.1 129O1a ES cells, replacing exons 11–21 of the $Ca_V3.3$ gene with the expression/selection cassette indicated in Fig. 1. For target construction, the 5′ and 3′ homology arms (~5.1 kb XhoI and ~4.5 kb EcoRV/BamHI restriction fragments, respectively) were cloned from a 129SVJ genomic BAC library and placed on either side of the expression/selection cassette shown in Fig. 1. Homologous recombination in G418-resistant ES cells at the 5′ and 3′ ends of the target locus was determined by Southern blot of EcoRV (WT 17 kb/mutant 10 kb) and EcoRI (WT 17 kb/mutant 8 kb) digested ES cell genomic DNA, respectively, using external probes. The PGK Neo MC1 tk selection cassette was removed by transient pCAG-Cre transfection of targeted cells followed by selection with gancyclovir (2 μM). Targeted ES cell clones were injected into C57BL/6J-derived blastocysts. Male chimaeras were crossed with C57BL/6J females to produce N1F0 offspring, which were backcrossed into the C57BL/6J line for seven generations and further intercrossed to produce homozygous mutant mice ($Ca_V3.3^{-/-}$). Details of genotyping and RT-PCR are given in *SI Materials and Methods*.

Electrophysiology and Fluorescent Imaging. For whole-cell patch clamp recordings and fluorescent Ca^{2+} imaging in nRt cells, horizontal slices 300 μm thick were prepared from 3- to 4-wk-old and 8- to 10-wk-old $Ca_V3.3^{-/-}$ mice and WT littermates, as previously described (16). For extracellular multiunit recordings, slices 400 μm thick were prepared from 6- to 8-wk-old mice and maintained in an interface-style recording chamber at near-physiological temperature (30–32 °C). Details of electrophysiological recording conditions, fluorescence imaging, and data acquisition and analysis are given in *SI Materials and Methods*.

EEG/EMG Recordings. Female 8- to 9-wk-old $Ca_V3.3^{-/-}$ mice and WT littermates maintained under 12:12-h light/dark schedule (lights on at 8:00 AM) were implanted with EEG and EMG electrodes according to standard procedures (16). $Ca_V3.3^{-/-}$ mice showed comparable locomotor activity across the 24-h light-dark cycle (Fig. S5). Under deep ketamine/xylazine anesthesia (i.p., 100 mg/kg and 10 mg/kg, respectively, at a volume of 8 μL/g), six gold-plated miniature screws (1.1-mm diameter) were implanted into the skull. The two screws placed over the right frontal and right parietal cortex served as EEG electrodes. For EMG measurements, two semirigid gold wires were inserted into the neck muscles, and all electrodes were soldered to a connector. The construct was fixed to the skull using the four additional screws and sealed with dental cement. After 4–7 d of recovery from surgery, animals were tethered to the recording leads and a commutator (Dragonfly). Four or five additional days were allowed for habituation. Undisturbed sleep–wake behavior was recorded for 48 h. Further details of recording, scoring, and data analysis are given in *SI Materials and Methods*.

Statistical Analysis. Data are presented in all figures as mean ± SEM. A paired or unpaired Student's *t* test was used as appropriate with significance accepted for $P < 0.05$.

ACKNOWLEDGMENTS. We are indebted to Dr. A. Feltz for first alerting us to the $Ca_V3.3^{-/-}$ mouse. We are grateful to Drs. M. Geppert and A. Randall for supervisory advice during knockout mouse generation; to Drs. I. Gloger, S. Harrison, and J. Latcham for their support; and to Dr. C. Davies for acting as a GlaxoSmithKline referent. We thank E. Grau and T. Hamilton for performing blastocyst microinjection, F. Faggioni for carrying out RNA expression analysis, and M. Trenkoska-Olmo for excellent animal caretaking. We thank Dr. S. Maret and all laboratory members for critical reading of the manuscript. This work was supported by Synapsis Foundation (S.A.), by the National Institutes of Health (J.P.A.), and by the Swiss National Science Foundation (A.L.).

1. Perez-Reyes E (2003) Molecular physiology of low-voltage-activated T-type calcium channels. *Physiol Rev* 83:117–161.
2. Klöckner U, et al. (1999) Comparison of the Ca^{2+} currents induced by expression of three cloned α1 subunits, α1G, α1H and α1I, of low-voltage-activated T-type Ca^{2+} channels. *Eur J Neurosci* 11:4171–4178.
3. Lee JH, et al. (1999) Cloning and expression of a novel member of the low voltage-activated T-type calcium channel family. *J Neurosci* 19:1912–1921.
4. Talley EM, et al. (1999) Differential distribution of three members of a gene family encoding low voltage-activated (T-type) calcium channels. *J Neurosci* 19:1895–1911.
5. Broicher T, Kanyshkova T, Meuth P, Pape HC, Budde T (2008) Correlation of T-channel coding gene expression, I_T, and the low threshold Ca^{2+} spike in the thalamus of a rat model of absence epilepsy. *Mol Cell Neurosci* 39:384–399.
6. Crandall SR, Govindaiah G, Cox CL (2010) Low-threshold Ca^{2+} current amplifies distal dendritic signaling in thalamic reticular neurons. *J Neurosci* 30:15419–15429.
7. Joksovic PM, Bayliss DA, Todorovic SM (2005) Different kinetic properties of two T-type Ca^{2+} currents of rat reticular thalamic neurones and their modulation by enflurane. *J Physiol* 566:125–142.
8. Anderson MP, et al. (2005) Thalamic $Ca_v3.1$ T-type Ca^{2+} channel plays a crucial role in stabilizing sleep. *Proc Natl Acad Sci USA* 102:1743–1748.
9. Lee J, Kim D, Shin HS (2004) Lack of delta waves and sleep disturbances during non-rapid eye movement sleep in mice lacking $\alpha1_G$-subunit of T-type calcium channels. *Proc Natl Acad Sci USA* 101:18195–18199.
10. Bourinet E, et al. (2005) Silencing of the $Ca_v3.2$ T-type calcium channel gene in sensory neurons demonstrates its major role in nociception. *EMBO J* 24:315–324.
11. Liu XB, Murray KD, Jones EG (2011) Low-threshold calcium channel subunit $Ca_v3.3$ is specifically localized in GABAergic neurons of rodent thalamus and cerebral cortex. *J Comp Neurol* 519:1181–1195.
12. Huguenard JR, Prince DA (1992) A novel T-type current underlies prolonged Ca^{2+}-dependent burst firing in GABAergic neurons of rat thalamic reticular nucleus. *J Neurosci* 12:3804–3817.
13. Joksovic PM, et al. (2006) $Ca_v3.2$ is the major molecular substrate for redox regulation of T-type Ca^{2+} channels in the rat and mouse thalamus. *J Physiol* 574:415–430.
14. Steriade M (2006) Grouping of brain rhythms in corticothalamic systems. *Neuroscience* 137:1087–1106.
15. Guillery RW, Feig SL, Lozsádi DA (1998) Paying attention to the thalamic reticular nucleus. *Trends Neurosci* 21:28–32.
16. Cueni L, et al. (2008) T-type Ca^{2+} channels, SK2 channels and SERCAs gate sleep-related oscillations in thalamic dendrites. *Nat Neurosci* 11:683–692.
17. Paz JT, Christian CA, Parada I, Prince DA, Huguenard JR (2010) Focal cortical infarcts alter intrinsic excitability and synaptic excitation in the reticular thalamic nucleus. *J Neurosci* 30:5465–5479.
18. Beenhakker MP, Huguenard JR (2009) Neurons that fire together also conspire together: Is normal sleep circuitry hijacked to generate epilepsy? *Neuron* 62:612–632.
19. Lee JH, Gomora JC, Cribbs LL, Perez-Reyes E (1999) Nickel block of three cloned T-type calcium channels: Low concentrations selectively block α1H. *Biophys J* 77:3034–3042.
20. Zaman T, et al. (2011) $Ca_v2.3$ channels are critical for oscillatory burst discharges in the reticular thalamus and absence epilepsy. *Neuron* 70:95–108.
21. Chevalier M, Lory P, Mironneau C, Macrez N, Quignard JF (2006) T-type $Ca_V3.3$ calcium channels produce spontaneous low-threshold action potentials and intracellular calcium oscillations. *Eur J Neurosci* 23:2321–2329.
22. Vyazovskiy VV, Achermann P, Borbély AA, Tobler I (2004) The dynamics of spindles and EEG slow-wave activity in NREM sleep in mice. *Arch Ital Biol* 142:511–523.
23. Franken P, Malafosse A, Tafti M (1998) Genetic variation in EEG activity during sleep in inbred mice. *Am J Physiol* 275:R1127–R1137.
24. Cain SM, Snutch TP (2010) Contributions of T-type calcium channel isoforms to neuronal firing. *Channels (Austin)* 4:475–482.
25. Morison RS, Bassett DL (1945) Electrical activity of the thalamus and basal ganglia in decorticate cats. *J Neurophysiol* 8:309–314.
26. Crunelli V, Hughes SW (2010) The slow (<1 Hz) rhythm of non-REM sleep: A dialogue between three cardinal oscillators. *Nat Neurosci* 13:9–17.
27. Espinosa F, Torres-Vega MA, Marks GA, Joho RH (2008) Ablation of $K_v3.1$ and $K_v3.3$ potassium channels disrupts thalamocortical oscillations *in vitro* and *in vivo*. *J Neurosci* 28:5570–5581.
28. Becker AJ, et al. (2008) Transcriptional upregulation of $Ca_v3.2$ mediates epileptogenesis in the pilocarpine model of epilepsy. *J Neurosci* 28:13341–13353.
29. Fogel SM, Smith CT (2011) The function of the sleep spindle: A physiological index of intelligence and a mechanism for sleep-dependent memory consolidation. *Neurosci Biobehav Rev* 35:1154–1165.
30. Khazipov R, Luhmann HJ (2006) Early patterns of electrical activity in the developing cerebral cortex of humans and rodents. *Trends Neurosci* 29:414–418.
31. Rosanova M, Ulrich D (2005) Pattern-specific associative long-term potentiation induced by a sleep spindle-related spike train. *J Neurosci* 25:9398–9405.